CrossMark

ORIGINAL PAPER

Wave Propagation in Isotropic Media with Two Orthogonal Fracture Sets

S. Shao[1] · L. J. Pyrak-Nolte[1,2,3]

Abstract Orthogonal intersecting fracture sets form fracture networks that affect the hydraulic and mechanical integrity of a rock mass. Interpretation of elastic waves propagated through orthogonal fracture networks is complicated by guided modes that propagate along and between fractures, by multiple internal reflections, as well as by scattering from fracture intersections. The existence of some or all of these potentially overlapping modes depends on local stress fields that can preferentially close or open either one or both sets of fractures. In this study, an acoustic wave front imaging system was used to examine the effect of bi-axial loading conditions on acoustic wave propagation in isotropic media containing two orthogonal fracture sets. From the experimental data, orthogonal intersecting fracture sets support guided waves that depend on fracture spacing and fracture-specific stiffnesses. In addition, fracture intersections have stronger effects on propagating wave fronts than merely the superposition of the effects of two independent fractures because of energy partitioning among transmitted/reflected waves, scattered waves and guided modes. Interpretation of the properties of fractures or fracture sets from seismic measurements must consider non-uniform fracture stiffnesses within and among fracture sets, as well as considering the striking effects of fracture intersections on wave propagation.

✉ L. J. Pyrak-Nolte
  ljpn@purdue.edu

1   Department of Physics, Purdue University, West Lafayette, IN, USA

2   School of Civil Engineering, Purdue University, West Lafayette, IN, USA

3   Department of Earth, Atmospheric and Planetary Sciences, Purdue University, West Lafayette, IN, USA

1 Introduction

Many engineering activities require knowledge of the isotopic or anisotropic properties of rock for the design of underground excavations, foundations, and adits, as well as for rock strength analysis (Amadei 1996). Stress determined from strain measurements can be misinterpreted if an anisotropic rock is assumed to be isotropic. For example, Amadei and Goodman (1982) showed for overcoring techniques that the magnitude and direction of stress for a transversely isotropic medium would be misinterpreted by as much as 50 % and 100 degrees, respectively, if isotropy was assumed. One method used to interpret the anisotropic nature of rock is from the measurement of compressional and shear wave velocities that depend on the elastic moduli of a sample. While many investigations have studied the effects of single fractures, a set of parallel fractures and orthogonal fractures on elastic wave velocities and elastic properties (Abell et al. 2014; Bakulin et al. 2000; Carcione and Picotti 2012; Fuck and Tsvankin 2006; Hood and Schoenberg 1989; Pyrak-Nolte et al. 1990a, b; Schoenberg 1980; Schoenberg and Douma 1988; Schoenberg and Helbig 1997), the effect of intersections on a propagating wave has been largely ignored.

Intersecting fractures occur in nature when two or more fractures have different orientations. Orthogonal fracture sets are a special case of mutually perpendicular (dihedral angle $\sim 90°$) sets that typically occur in horizontal strata. The formation of orthogonal fracture sets has been attributed to bi-axial tectonic extensions, bending of a system from local loading or differential compaction of a rock unit

with a set of parallel fractures, elastic Poisson cross-strain effect, or from a triaxial remote loading (Bai et al. 2002; Mandl 2005). While orthogonal fractures sets are commonly observed (Bai et al. 2002; Braun and Kelemen 2002; Gross 1993; Hobday and Worthington 2012; Hodgson 1961; Mandl 2005; Stearns 1972), research on elastic wave propagation in fractured media has mostly focused on single fractures and sets of parallel fractures. Single fractures have been shown, theoretically and experimentally, to delay and attenuate waves (Angel and Achenbach 1985; Choi et al. 2014; Gu et al. 1996; Lubbe and Worthington 2006; Nakagawa et al. 2000a; Pyrak-Nolte et al. 1990b; Schoenberg 1980). The magnitude of the delay and the attenuation depend on the frequency of the signal, ω, fracture-specific stiffness, κ, (inverse of fracture compliance) and the seismic impedance (Z = density × phase velocity) of the rock matrix. Fracture-specific stiffness captures the state of coupling between the fracture walls and depends on the amount of contact between the two surfaces as well as on the aperture distribution (Cook 1992; Goodman et al. 1968; Hopkins 1990; Kendall and Tabor 1971; Myer 2000; Petrovitch et al. 2013; Petrovitch et al. 2014). Single fractures also support fracture interface waves (coupled Rayleigh waves) that are guided along a fracture plane (Gu 1994; Murty and Kumar 1991; Pyrak-Nolte and Cook 1987; Pyrak-Nolte et al. 1992; Shao and Pyrak-Nolte 2013). The existence and velocity of fracture interface waves also depend on Z, ω, and κ.

For a set of parallel fractures, each individual fracture affects a propagating three-dimensional wave front and can introduce additional wave interference effects (e.g., stop-band behavior) that arise from the spacing between fractures and that depend on Z, ω, and κ of the fractures in the set (Nakagawa et al. 2000b). Wave-guiding can also occur between two fractures (Nakagawa et al. 2002; Nihei et al. 1994, 1999; Shao et al. 2015; Xian et al. 2001). While wave-guiding is known to arise from impedance contrasts in layered media, parallel fractures in isotropic media have also been shown to produce guided modes (Xian et al. 2001). Parallel fractures form planar wave-guides that trap energy between fractures. A wave propagating parallel to the fractures is internally reflected between the fractures, leading to constructive and destructive interference with the direct wave. The existence and strength of such guided modes depend on the wavelength of the signal, on the fracture-specific stiffness and on the spacing between two consecutive fractures. Shao et al. (2015) demonstrated experimentally and theoretically that compressional-wave-guided modes supported by a set of parallel fractures in an anisotropic layered medium can obscure the presence of layering. From their study, the number of guided modes and the delay for each mode depended not only on ω and κ,

but also on the orientation of the fracture set relative to the layering in an anisotropic medium.

An additional level of complexity is encountered in media with two orthogonal fracture sets. First, the wave-guides formed by the fractures are rectangular. The shape of a wave-guide affects arrival time, phase shifts, and amplitudes of the guided modes. In sedimentary rocks, orthogonal or cross fracture sets form rectangular wave-guides with a wide range of horizontal/vertical fracture spacings from 10 mm to 1 m (Gross 1993). Second, intersections exist between the fractures. For an orthogonal fracture network, intersections are long linear features that can lead to additional scattering and energy loss. Although some numerical studies showed that intersections have little or no influence on elastic wave propagation (Grechka and Kachanov 2006), recent theoretical work demonstrated that fracture intersections can support guided modes that, just like single fractures, depend on frequency and the coupling at the intersection (Abell 2015; Abell and Pyrak-Nolte 2013). Furthermore, Abell (2015) showed experimentally that fracture intersections support guided modes that are highly localized to the intersection and exhibit distinct particle motions. Orthogonal fracture networks may be subjected to non-uniform stress fields depending on local tectonic conditions or subsurface engineering activities, which can result in different specific stiffnesses between two fracture sets and/or among the fractures in each set. The existence of some or all of these potentially overlapping structural features, the existence of attenuation/scattering mechanisms and the effect of local stress fields that can preferentially close or open either one or both sets of fractures or intersections, will contribute to the measured wave field and affect the interpretation of the data.

In this study, we demonstrate, experimentally, that (1) orthogonal fracture sets support guided modes, (2) non-uniform stiffnesses among the fractures result in non-uniform delays and attenuation of the propagating wave front, and (3) fracture intersections attenuate and delay propagating modes more than that expected from the superposition of the effects of 2 fractures, and hence intersections constitute a new structural element that must be included explicitly in seismic scattering studies.

2 Experimental Approach

2.1 Samples

Four cubic aluminum samples (100 mm × 100 mm × 100 mm) were used to investigate the effect of two orthogonal fracture sets on a propagating acoustic wave

front. Three of the samples contained horizontal and vertical fracture (Fig. 1). Samples F2020 and F1010 have equal fracture spacings in the two orthogonal directions of 20 and 10 mm, respectively (Fig. 1a, b). Sample F1020 has a horizontal fracture spacing of 20 mm and a vertical spacing of 10 mm (Fig. 1c). The fractures were cut with a band saw and machined to be smooth. An intact aluminum block with the same external dimensions as the samples with fracture networks (Fig. 1d) was used as a standard.

2.2 Acoustic Wave Front Imaging

Acoustic wave front imaging is a traditional method for recording the distribution of energy in an arriving wave front and to visualize the effect of textural and structural components of a sample on a propagating wave front (Abell et al. 2014; Hauser et al. 1995; Nagy et al. 1995; Oliger et al. 2003; Pyrak-Nolte et al. 1996; Shao et al. 2015; Xian et al. 2001). Most previous studies examined
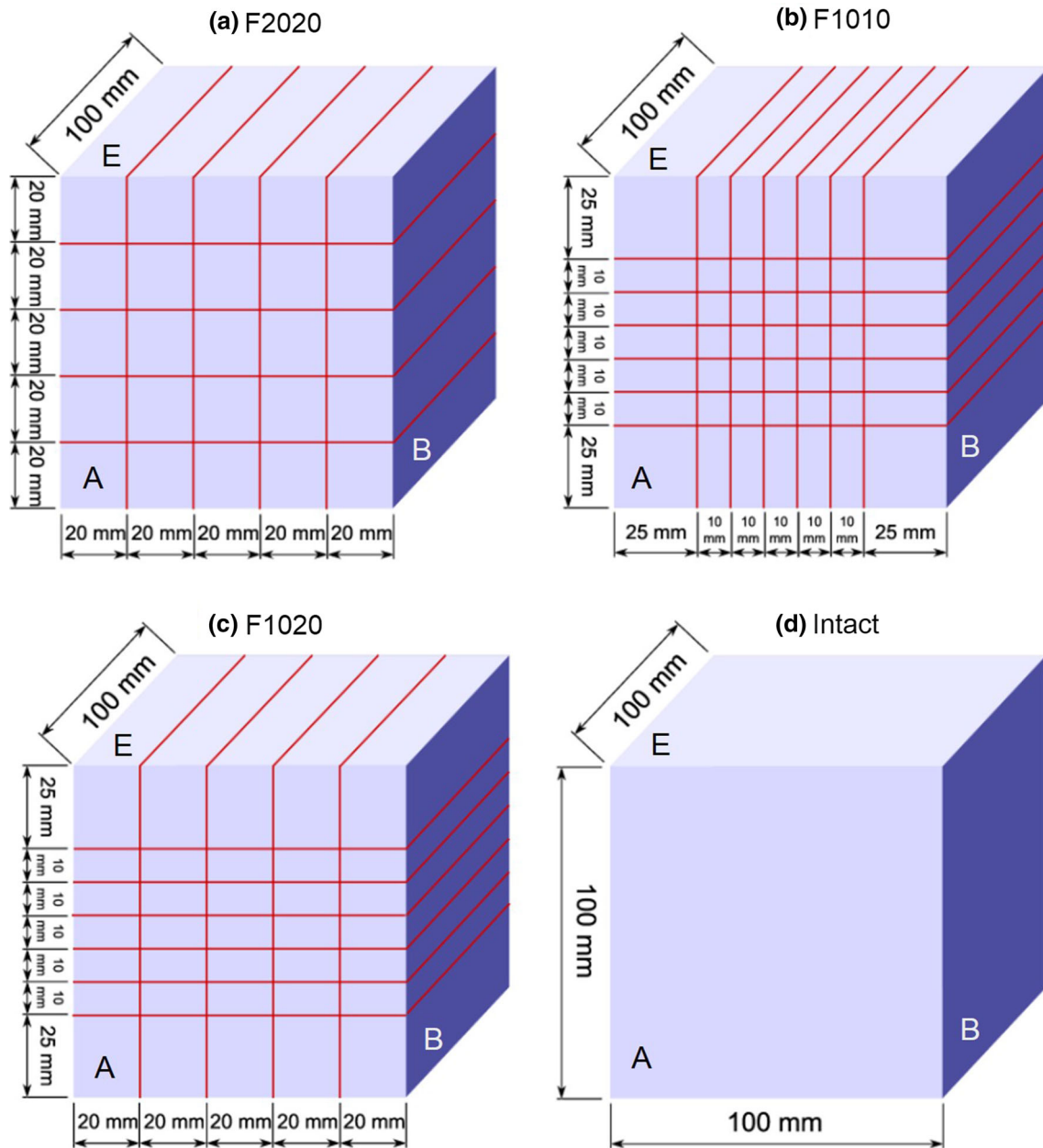

Fig. 1 Sketches of aluminum samples: **a** F2020 with horizontal and vertical fracture spacings both equal to 20 mm, **b** F1010 with both horizontal and vertical fracture spacings equal to 10 mm, **c** F1020 with vertical and horizontal fracture spacings of 10 and 20 mm, respectively, **d** an intact sample with no fractures. *Red lines* indicate the locations of fractures (color figure online)

wave propagation on samples either subjected to no load or to a uniaxial load. Working with orthogonal fracture sets requires bi-axial loading conditions to maintain the cohesiveness of the sample and to change the specific stiffness of the fractures in both sets. A wave front imaging system with bi-axial load-control was designed and used for this study (Fig. 2). The system consists of (a) A Soil Test 445kN load frame to apply a normal load on the horizontal fracture set; (b) a custom built, manually controlled 222 kN load frame with a Parker actuator and an Interface, model 1220AF-50 K-B, 222 kN load cell to apply a load normal to plane of the vertical fracture set; (c) an aluminum tank with pistons to hold the water needed for water-coupling during the acoustic measurements; (d) two linear actuators (Newport Model 850B) to translate the receiver, controlled by a Newport ESP 300 motion controller; (e) two spherically focused water-coupled piezoelectric transducers (broadband with a central frequency of 1 MHz) to send and receive the signals; (f) a pulse generator (Panametrics model 5077PR) to generate signals; and (g) a digital oscilloscope (NI USB-5133) to record signals that are stored on a computer. Additional details can be found in (Shao 2015).

To perform an experiment, the sample is first sealed with clear tape to prevent water invasion along fracture planes as samples are submerged in water in the aluminum tank during testing. Sample corners and tape seams were also sealed with Coghlans 8880 Airstop, a commercial liquid sealant, and dried for at least 1 h prior to testing. The intact sample was also sealed in the same manner to
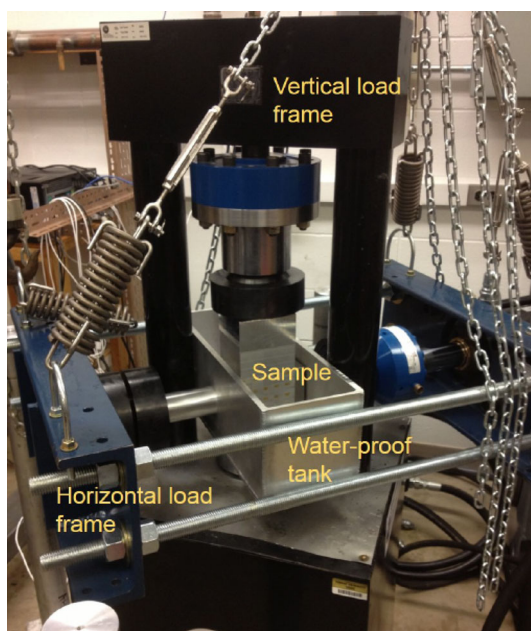
**Fig. 2** Bi-axial loading components of the acoustic wave front imaging system

quantify any effects of sealing on the wave front. During the experiments, equal loads were applied vertically from face E to F (opposite to E, Fig. 1) and horizontally from face B to D (opposite to B, Fig. 1). The source transducer was held at a fixed position on the center of the sample (Face A in Fig. 1), while the receiving transducer was translated over a 60 mm by 60 mm region of the sample in 1-mm increments (on Face C which is opposite to Face A) to map out the arriving wave front as a function of time. A pulse generator sent an excitation pulse (400 V square pulse) to the source transducer. The pulse width was 0.3 μs with a repetition rate of 100 Hz. A transmitted wave signal was recorded at each receiver position representing a 100-μs window with a fixed time delay (e.g., 30 μs) at a sampling rate of 10^8 per second. 3600 signals were recorded during each test. A 3D dataset of the transmitted wave front was recorded with two spatial and one temporal dimension (i.e., 60 mm × 60 mm × 100 μs).

3 Results

Examples of the type of information acquired with wave front imaging are shown in Fig. 3 for the intact sample. In this paper, the central waveforms (when the source and receiver are aligned) from each data set are used to examine the effect of fracture-specific stiffness and fracture spacing on waves guided between fractures (Fig. 3b). Snapshots of a wave front in time (x–y plane in Fig. 3a) are used to determine the effect of fractures and fracture intersections on a propagating wave front. The color represents the amplitude of the signal with blue representing negative amplitudes and red positive amplitudes. Data taken over one spatial dimension as a function of time are used for determining the time delay caused by fractures and fracture intersections (y-time plane or x-time plane in Fig. 3a).

For the isotropic intact sample, the wave front spreads out uniformly in all directions (Fig. 3a). Conversely, the energy distribution in the fractured samples depends on the fracture spacing, number of fractures, and the applied loads. Figures 4, 5, and 6 show snapshots of the wave front from samples F2020, F1010, and F1020, respectively, for four applied stresses, 0.4, 2.0, 4.0, and 6.0 MPa. The snapshots were taken at the same time after the first arrival for these samples. Under low-stress conditions, the wave front is strongly confined and localized to the central block in which the waves were launched. The strong energy confinement occurs because the fracture-specific stiffness or coupling between the fracture surfaces is weak, and very little energy is transmitted across the fractures. As more stress is applied to the sample and fracture-specific stiffness increases, the

Fig. 3 Data visualization of the 3D measured acoustic wave fronts (**a**) and the central waveform (**b**) from the intact sample
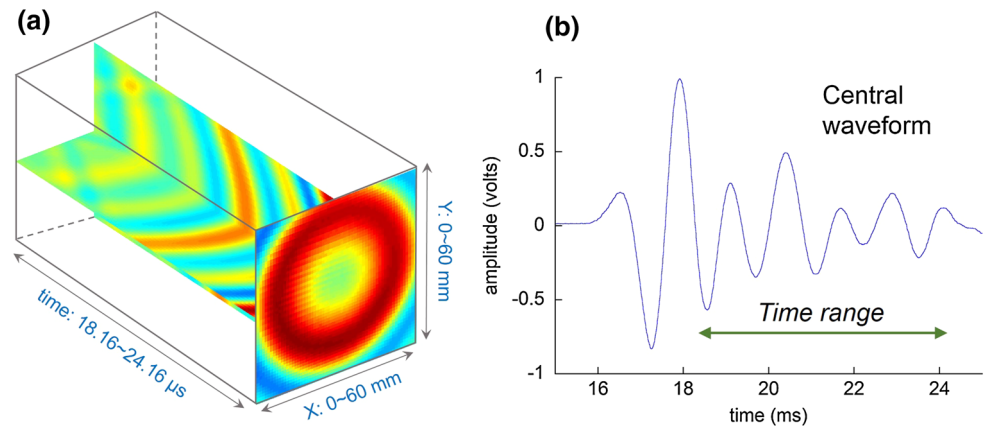

Fig. 4 2D snapshots of the acoustic wave front in time for bi-axial stresses of **a** 0.4 MPa, **b** 2.0 MPa, **c** 4.0 MPa, and **d** 6.0 MPa for the F2020 sample. *Dashed lines* indicate the fractures
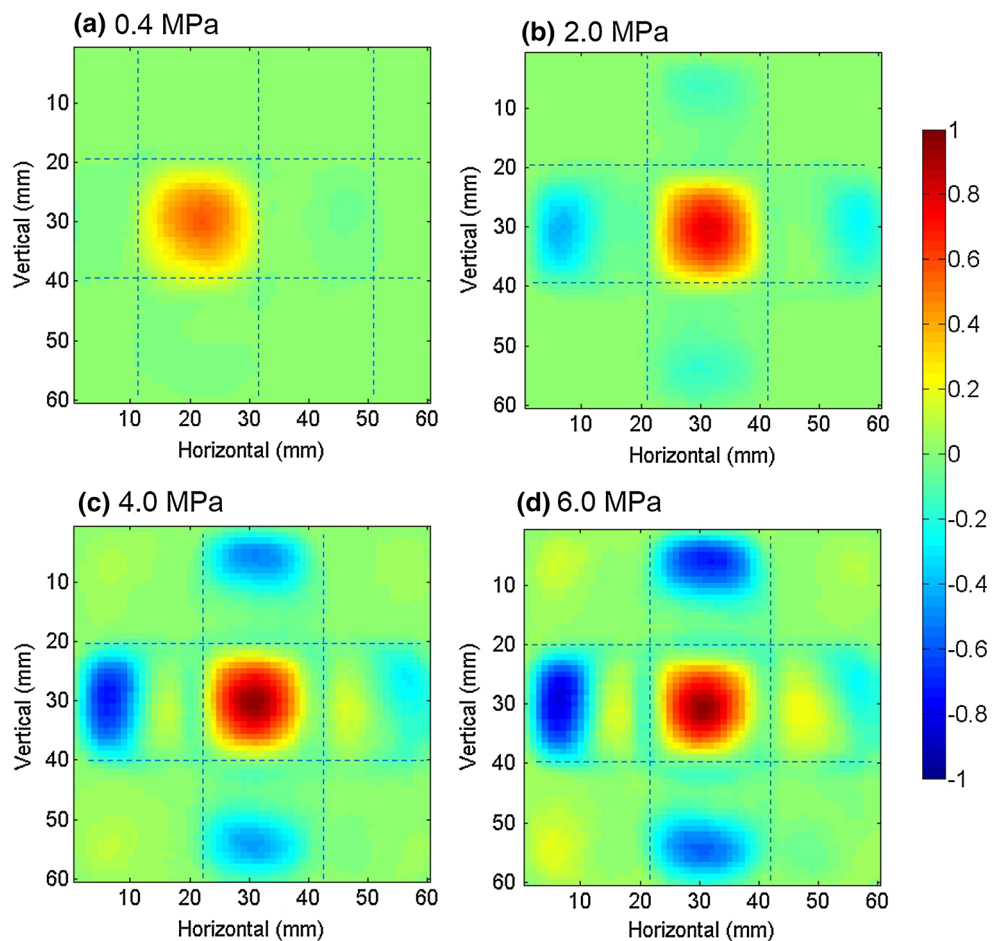
transmission across the fractures increases and is observed to propagate farther into the sample. For example, for sample F1010, when the stress was increased to 2 MPa (Fig. 5b), the energy is observed to propagate across the fractures that define the central block into neighboring blocks. When the stress was increased to 4 and 6 MPa (Fig. 5c, d), the energy that propagated across the fractures increased in amplitude. Phase contrasts between neighboring blocks were clearly observed, and fracture-

network geometry or block size between fractures was clearly delineated under high loading conditions (Figs. 4, 5, 6). The wave front images also show that energy transmission was not uniform across the different fractures in the network (e.g., sample F2020 in Fig. 4 or samples F1010 or F1020 in Figs. 5 and 6). The variation in transmitted amplitude indicates that fracture-specific stiffnesses among the fractures in the network differed, even for applied bi-axial loads with equal magnitudes.

Fig. 5 2D snapshots of the acoustic wave front in time for bi-axial stresses of **a** 0.4 MPa, **b** 2.0 MPa, **c** 4.0 MPa, and **d** 6.0 MPa for the F1010 sample. *Dashed lines* indicate the fractures
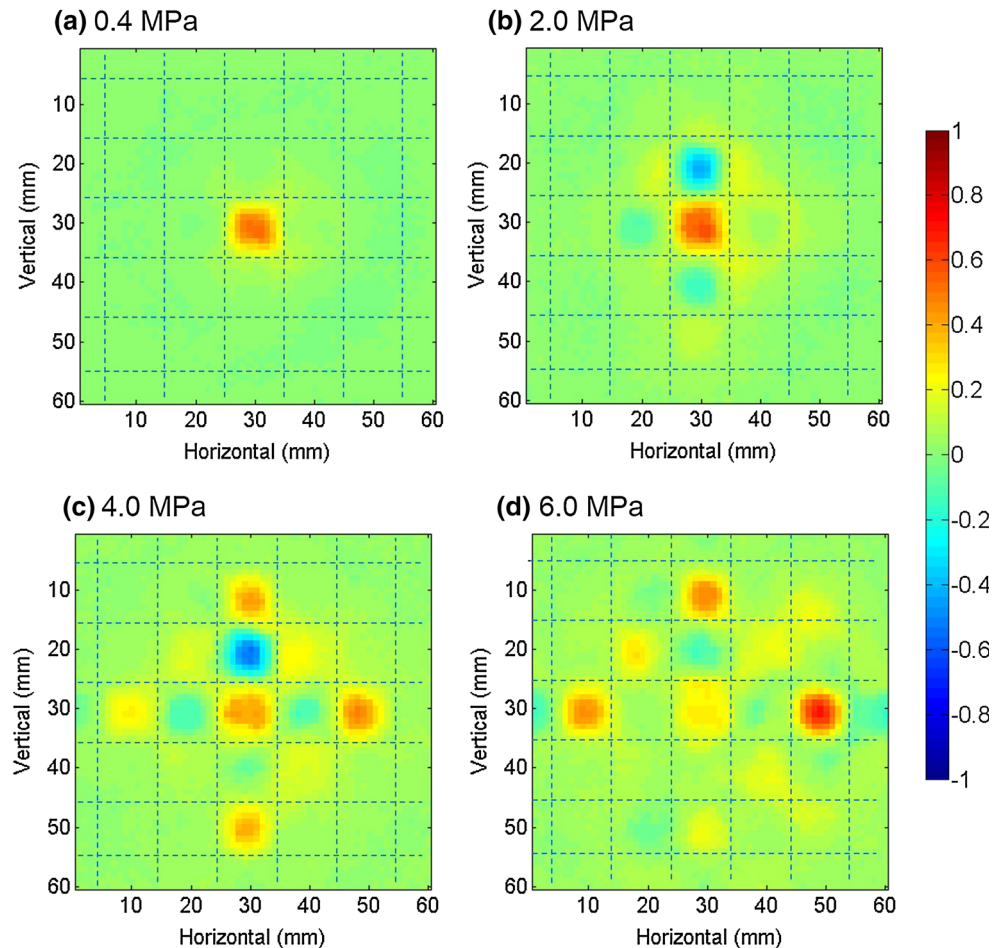

The effect of fracture intersections and the individual fractures in the network on a propagating wave front is shown in Fig. 7 from a comparison of signals propagated a fixed distance from the source (Fig. 7, insets). Signals propagated the same distance in the intact sample are shown in Fig. 7a, and their locations are given by the red dots in Fig. 7a (inset). As expected for a uniform isotropic sample, the arrival time and amplitude of the direct wave (first arrival) are uniform. Signals propagated across a single fracture (red signals) and across a fracture intersection (blue signals) are shown in Fig. 7b, c for sample F2020. The positions on the sample where the signals were recorded are shown by the red and blue dots on the drawing of the imaged region of the sample (inset in Fig. 7). The positions were selected to have the same travel path length as that for the intact sample. Fracture intersections strongly attenuated the amplitude of the signal at both low (0.4 MPa) and high (4.0 MPa) bi-axial stresses, though a slight increase in amplitude is observed at high stress. Signals propagated across a fracture increased significantly with an increase in stress. The fracture-specific stiffness differed between the vertical and horizontal fractures as indicated by the differences in amplitude and arrival time for waves propagated across these fractures.

4 Discussion

The wave front imaging data showed that (a) energy is confined in blocks defined by two orthogonal fracture sets, (b) the fracture-specific stiffness varied among the fractures within a set and between fracture sets, and (c) that fracture intersections strongly attenuate and delay propagating waves. In this section, we address these three observations with currently available theoretical approaches and analyses.

4.1 Wave-Guiding

Previous studies demonstrated theoretically and experimentally that wave-guiding between parallel fractures is controlled by the ratio of the acoustic wavelength to fracture spacing, fracture-specific stiffness, and matrix properties (Shao et al. 2015; Xian et al. 2001). Wave-guiding between two fractures is illustrated in Fig. 8. From theory, the wave-guiding condition requires constructive interference between the original wave and the twice-reflected wave. A monochromatic plane wave with wavelength, λ, and phase velocity, v, is reflected from the upper fracture
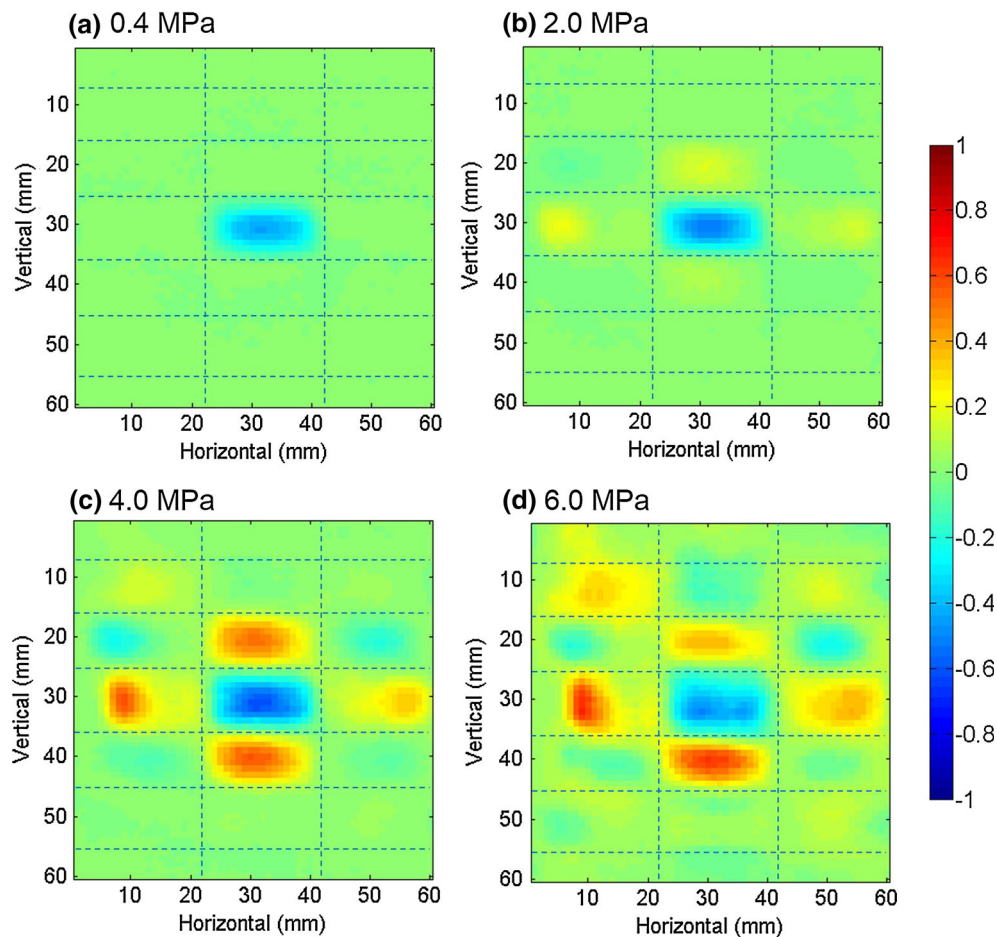
Fig. 6 2D snapshots of the acoustic wave front in time for bi-axial stresses of **a** 0.4 MPa, **b** 2.0 MPa, **c** 4.0 MPa, and **d** 6.0 MPa for the F1020 sample. *Dashed lines* indicate the fractures

and then reflected a second time from the lower fracture plane. This twice-reflected wave propagates in the same direction as the original wave leading to constructive and destructive interference. The wave-guiding condition requires the phase difference between the original and the reflected wave to be an integer multiple of 2π. For wave-guiding between fractures, the phase difference includes a geometrical component related to the path length of the reflected waves and a dynamic component related to the phase shift upon each reflection from a fracture (Shao et al. 2015; Xian et al. 2001). The phase shift upon reflection depends on the matrix properties, the fracture-specific stiffness, and the signal frequency. These previous studies showed that as fracture-specific stiffness increases, the time delay upon reflection decreases, the number of modes decrease for a given frequency band, and less energy is confined in the wave-guide as more energy is transmitted across the fractures and out of the wave-guide. Guided modes between fractures tend to be leaky.

While the theory for a rectangular wave-guide bounded by fractures and intersections has not yet been derived,

signatures of wave-guiding are observed in the data from the samples with orthogonal fracture sets. Figure 9 provides a comparison of the central signals from all three fractured aluminum samples (F2020, F1010 and F1020) for stresses of 0.4, 2.0, and 4.0 MPa. Fracture spacing (or shape of the central block/wave-guide) affects the transmitted signal. For example, the signal from F2020 exhibits a strong first arrival that is not observed for samples F1010 and F1020. Also note that the succeeding wave packets for all three samples differ in arrival times, frequency, and amplitudes. These differences arise from the size and shape of the waveguide, defined by the vertical and horizontal fracture spacing, and from the stiffnesses of the fractures that bound the rectangular wave-guide. The geometry of the wave-guide affects the geometric component of the time delay (i.e., differences in path length) that contributes to the phase shift that causes constructive/destructive interference and affects the amplitude of the guided mode. The signal from sample F2020 exhibited the cleanest and strongest first arrival because the geometric path length was the largest of the three samples. In Sample F2020, the
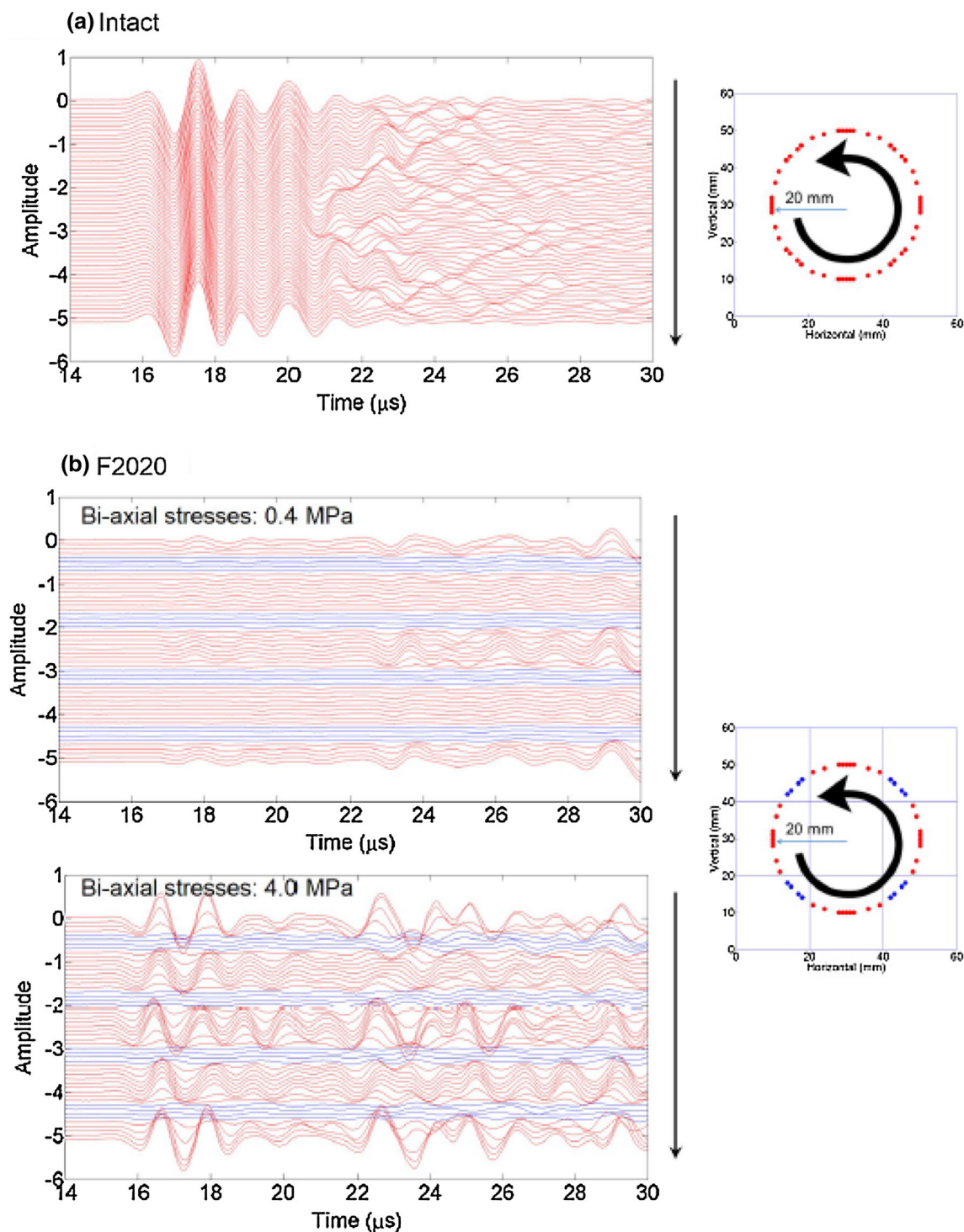
Fig. 7 Transmitted signals taken from the same distance (20 mm) to center from **a** the Intact sample and **b** the F2020 sample at 0.4 and 4 MPa stress conditions. In **b** the blue signals propagated across an intersection

lowest order mode was sufficiently delayed and did not interfere with the first cycle of the direct wave. Strong destructive interference between the direct wave and the lowest order guided mode almost extinguishes the first arrival in the signals from samples F1010 and F1020.

The time delay and amplitude of guided modes is also affected by fracture-specific stiffness. The dynamic time delay results from the phase shift upon reflection from the fracture. For every reflection, the amount of energy that is transmitted across the fracture depends on κ. Studies on
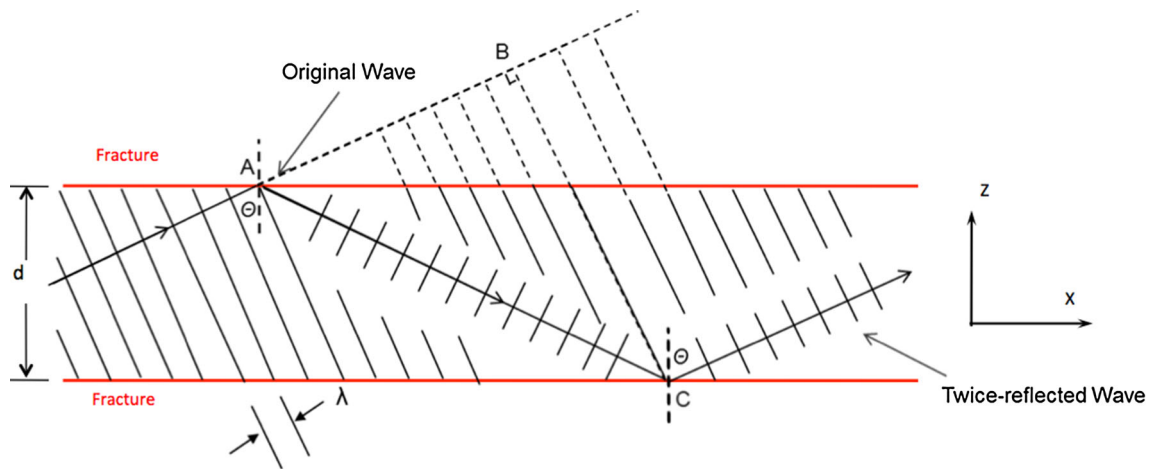
Fig. 8 A schematic drawing of the wave-guiding condition for two parallel fractures (shown in *red*) (color figure online)
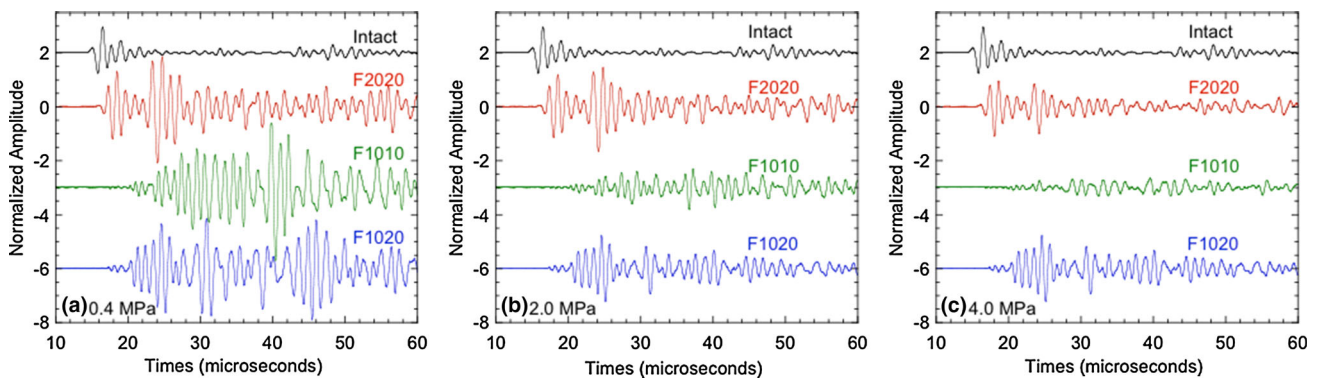
Fig. 9 Central waveforms for F2020, F1010 and F1020 for bi-axial stresses of **a** 0.4 MPa, **b** 2.0 MPa and **c** 4.0 MPa

single fractures have shown that wave transmission across a fracture increases as κ increases (Far et al. 2014; Lubbe et al. 2008; Pyrak-Nolte et al. 1990a, b; Shao et al. 2015; Xian et al. 2001). By increasing the bi-axial loads on the sample, the amount of energy confinement was reduced because the stiffness of the fractures increased. Fracture-specific stiffness increases when the contact between the two fracture surfaces increases (Greenwood and Williamson 1966; Hopkins et al. 1990; Kendall and Tabor 1971; Pyrak-Nolte et al. 1987). More energy was transmitted across the fractures at high stress than at low stresses leading to a reduction in amplitude in the guided modes with increasing stress.

The amplitudes of the different phases in the central waveforms were examined to delineate signal components associated with guided modes. Figure 10 shows peak-to-trough (P2P) amplitudes as a function of stress for Peaks 2–6 (see inset in Fig. 10) for the central waveforms from Sample F2020. The P2P amplitudes were normalized by the amplitude from Peak 1 as a function of bi-axial external stresses. Peak 1 is the direct bulk arrival (not reflected or guided), whose amplitude is independent of the fracture-
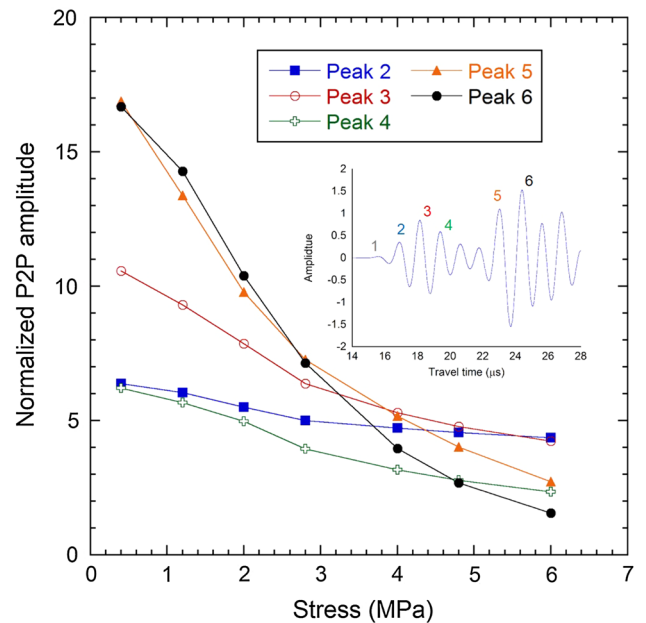
Fig. 10 Normalized P2P amplitudes for Peak 2–6 (inset, normalized by P2P amplitude of the first peak-direct arrival) as a function of bi-axial external stresses for sample F2020

specific stiffness. The amplitudes for Peaks 2–4 in the first wave packet did not decrease with increasing stress as dramatically as the amplitudes for Peaks 5 and 6 in the later arriving wave packet. Later arriving signals have been shown to contain higher-order guided modes in a system with a single set of parallel fractures (Shao 2015). Higher-order modes are more sensitive to fracture-specific stiffness because these modes reflect off the fracture more times than lower-order modes. Every time a mode is reflected off of a fracture, it loses energy, i.e., a portion of the energy is transmitted across the fracture where the amount transmitted is a function of fracture-specific stiffness and signal frequency. Lower-order guided modes (e.g., $m = 0$ or $m = 1$, see (Shao et al. 2015)) reflect fewer times and often overlap in time with the direct bulk arrival and can be difficult to distinguish or separate from the direct wave for short travel paths. Decoupling and quantifying time delays for each mode require theoretical work on rectangular wave-guides bounded by fractures. The solution for guided modes will increase in complexity if the fracture-specific stiffness of the two fracture sets is not equal and/or the fracture-specific stiffnesses vary among the fractures in each set.

4.2 Fracture-Specific Stiffness

As noted in the result section, snapshots of the acoustic wave front showed that energy transmitted across each individual fracture in a network was not uniform (Figs. 4, 5, 6), suggesting a variation in fracture-specific stiffness among the fractures in the network. An analysis was performed on signals from sample F2020 to estimate the specific stiffness of the fractures surrounding the

central wave-guide (Fig. 11a): horizontal upper (transmitted to A), horizontal lower (transmitted to C), vertical left (transmitted to B), and vertical right (transmitted to D). For these four locations, the wave traveled from the source focal point and was transmitted across a fracture to the receiver collection point. The displacement discontinuity theory (Nakagawa 1998; Pyrak-Nolte 1996; Pyrak-Nolte et al. 1990b; Schoenberg 1980) was used to estimate the stiffness of these four fractures from the data.

The benefits of using the displacement discontinuity theory are (1) the discreteness of a fracture is maintained such that waves are not delayed nor attenuated until crossing the fracture, (2) fracture-specific stiffness is an effective parameter that captures the complicated void topology that is linked to the mechanical and hydraulic response of a fracture (Petrovitch et al. 2013, 2014; Pyrak-Nolte and Nolte 2016), (3) frequency dependent group time delays, transmission and reflection coefficients arise from a purely elastic model, and (4) energy partitioning of waves into body waves arises and depends on fracture-specific stiffness. A disadvantage of this theoretical approach is that fractures are assumed to be infinite in extent and does not yield scattered modes from the edges or fracture tips. This disadvantage is often overcome in numerical methods by incorporating displacement discontinuity representations of finite-size fractures (De Basabe et al. 2010) or by explicit modeling of the physical geometry of the fracture (Petrovitch 2013; Shao et al. 2015).

The P-wave transmission coefficient was calculated from Eq. (1) as a function of frequency and fracture-specific stiffness for an incident angle of 78.7°, and assuming the seismic impedance, Z, of aluminum:

Fig. 11 **a** A snapshot of the wave front in sample F2020. **b** Fracture-specific stiffness for the 4 fractures surrounding the central wave-guide
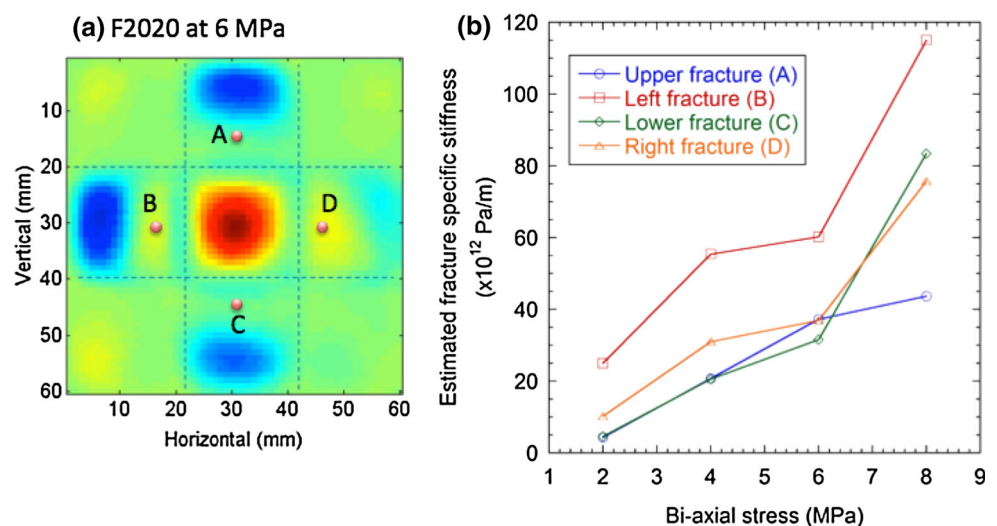
$$
\begin{bmatrix}
-\kappa_z \cos\theta_1 & \kappa_z \cos\phi_1 & -\kappa_z \cos\theta_2 + i\omega Z_P \cos 2\phi_2 & \kappa_z \sin\phi_2 - i\omega Z_S \sin 2\phi_2 \\
-\kappa_x \sin\theta_1 & -\kappa_x \cos\phi_1 & \kappa_x \sin\theta_2 - i\omega \dfrac{Z_S^2}{Z_P} \sin 2\theta_1 & \kappa_x \cos\phi_2 - i\omega Z_S \cos 2\phi_2 \\
-Z_P \cos 2\phi_1 & Z_S \sin 2\phi_1 & Z_{P2} \cos 2\phi_2 & -Z_S \sin 2\phi_2 \\
\dfrac{Z_S^2}{Z_P} \sin 2\theta_1 & Z_S \cos 2\phi_1 & \dfrac{Z_S^2}{Z_P} \sin 2\theta_2 & Z_S \cos 2\phi_2
\end{bmatrix}
\begin{bmatrix}
R_p \\ R_s \\ T_P \\ T_s
\end{bmatrix}
=
\begin{bmatrix}
-\kappa_z \cos\theta_1 \\
\kappa_x \sin\theta_1 \\
Z_P \cos 2\phi_1 \\
\dfrac{Z_S^2}{Z_P} \sin 2\theta_1
\end{bmatrix}
\tag{1}
$$

where θ and φ are the angles for the compressional, P, and shear, S, waves, respectively, and subscript 1 represents the medium that contains the incident and reflected waves, and subscript 2 represents the medium containing the transmitted waves. κ_z and κ_x represent the normal and shear stiffnesses of the fracture, respectively. Experimental P-wave transmission ratios were determined through spectral analysis, by dividing the spectral amplitude from a transmitted signal by that from the central signal, which only propagates in the solid part of the sample. The assumption was made that very little energy was lost when a wave propagated in the solid aluminum. Experimental results were fitted to the theory for a frequency range from 0.5 to 0.75 MHz, which spanned the spectral peak (dominant frequency) for a single fracture and was not significantly affected by other reflected/guided modes. With this method, fracture-specific stiffnesses were estimated for four fractures in sample F2020 (Fig. 11b) for different bi-axial stresses (yet equal in the vertical and horizontal directions). As the applied bi-axial load increased, fracture-specific stiffness increased (Fig. 11b). This provides a quantitative validation of the qualitative observation of the difference in fracture-specific stiffnesses among the fractures from the 2D snapshots in F2020 (Fig. 4b). For example, the specific stiffness of the left vertical fracture (B in Fig. 4a, b) is higher than the other three fractures (Fig. 11b). In Fig. 4, the wave energy transmitted across the left vertical fracture was observed to be higher than the energy transmitted through the other three fractures, especially at 4 MPa (Fig. 4c) and 6 MPa (Fig. 4d). At low stress, the stiffnesses of fractures A, C and D were 30–40 % of the stiffness of fracture B (Fig. 11b). At high stress, the stiffness of fractures C and D increased to 70 % of the stiffness measured for fracture B, while the stiffness for fracture A remained at 40 % of that measured for fracture B. The variation in fracture stiffness among fractures in a network will result in additional complexity in theoretical approaches for determining wave attenuation in fractured media.

4.3 Fracture Intersections

Recently, Abell (2015) showed theoretically and experimentally that a fracture intersection supports guided modes that are highly localized to the intersection and exhibit distinct particle

motions. These intersection waves, propagated along the intersection, are sensitive to the coupling along the intersection and result in energy partitioning between bulk and intersection waves. However, the effect of an intersection on wave transmission across an intersection has not been previously studied experimentally. The acoustic wave front datasets obtained here enable the observation and quantification of the effect of fracture intersections on the spectral content, amplitude and time delay of a propagating wave.

The spectra of waves propagated across a single fracture and across an intersection are compared to examine the seismic response of an intersection. A wavelet transformation (Nolte et al. 2000) was applied to signals propagated across an intersection, and across a single fracture (Fig. 12). Fractures behave as low-pass filters with a characteristic frequency $\omega_c = \kappa/Z$. As stress is applied to a fracture, the fracture stiffness increases thus increasing ω_c and enabling the transmission of higher frequency components. This behavior is observed in the spectra for the data from the single fracture (Fig. 12a) as well as in the spectra from waves propagated across an intersection (Fig. 12b). Waves propagated across a single fracture were larger in amplitude and had a higher peak (or dominant) frequency than the waves propagated across the fracture intersection. The intersection also behaves as a low-pass filter, but with a dominant frequency that is lower than that of the single fracture by a factor of ~ 2.

The increase in spectral amplitude of the waves propagated across an intersection with increasing stress indicates that the seismic response of an intersection is sensitive to the coupling along the intersection indicating that there is an effective "intersection stiffness." The amplitudes of the waves propagated across the intersection are smaller by a factor of 10 or more than the amplitudes from waves propagated across the single fracture. Theoretical calculations were performed using Eq. (1) to determine whether the observed attenuation across the intersection is simply equal to wave transmission across two fractures (i.e., using T_P^2 and assuming angles of incidence of 78.7° and 82° for the single fracture and the intersection, respectively). The analysis found that for the estimated fracture stiffness (Fig. 11) and frequency range of the data (Fig. 12), the amplitudes of the waves transmitted across the intersection should be smaller

Fig. 12 Spectra from waves propagated across *left* a single fracture and *right* across an intersection from sample F2020 for stresses of 2, 4 and 6 MPa
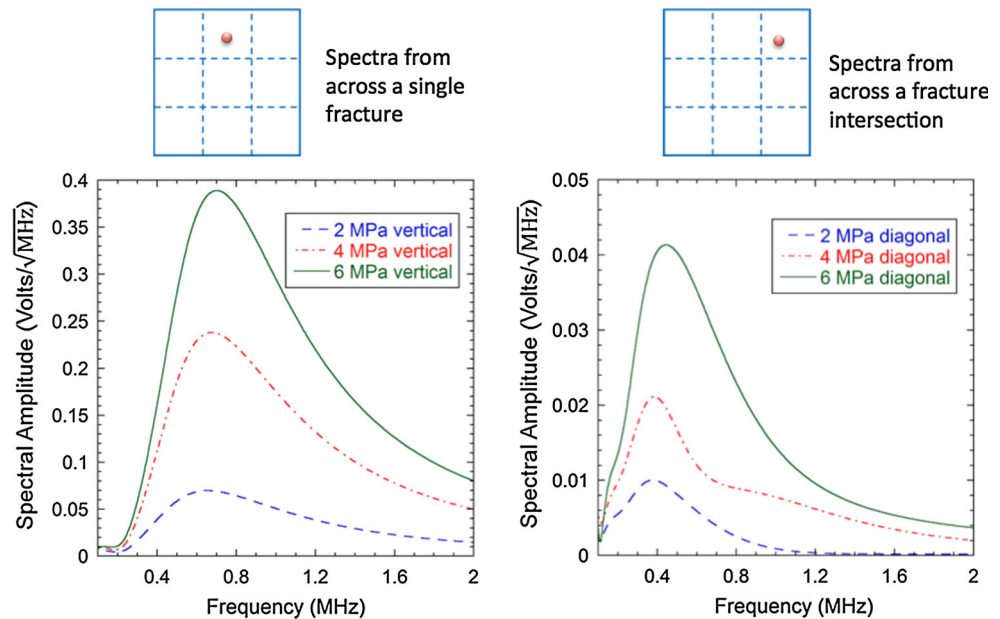
by a factor that ranges between 1.1 and 4 at most. The large attenuation observed in the measured data for the intersection arises from the energy partitioning into, and interference among, transmitted waves and guided waves (see Sect. 4.1). Currently, no theory exists for a wave impinging on an intersection that examines energy partitioning.

Single fractures delay propagating waves, and the magnitude of the group time delay depends on the Z, ω, and κ. The wave front imaging data were also used to examine the effect of fracture intersections and individual fractures on arrival times. Signal delays caused by the fractures in the network were determined and compared to the delays measured for waves propagated through the intact sample. From the 3D wave front imaging datasets for the intact and F2020 samples, the time delay for a series of waveforms along a line for each sample were determined (Fig. 13). The signals were taken from receiver positions along a vertical line that is horizontally 10 mm away from the center of the wave front (Fig. 13a). For the intact sample (Fig. 13b), the signals have uniform amplitudes and also exhibit a clear curvature in time delay that occurs because of the difference in travel path length between the source and receivers (Fig. 14a) as the signal delay increases for receiver positions farther from the center of the sample.

The effect of a single fracture and a fracture intersection on a propagating wave front is also shown in Fig. 13. Signals from sample F2020 (for the same receiver positions as for the intact sample) are shown in Fig. 13c–f for bi-axial stresses of 4, 8, 10, and 14 MPa, respectively. The signals shown in blue were recorded at the location of the fracture intersections. Signals at the same positions as the intersection are also shown in blue for the intact sample for comparison. At low stress, signals (blue) collected at a fracture

intersection were significantly delayed compared to the signals from the intact sample as well as at adjacent receiver positions on the fracture sample. At 4 MPa, the signal is delayed by half a cycle. As the bi-axial stress on the sample increased, the amplitudes of the waves propagated across the intersections increased and the arrival time decreased.

Relative time delays were quantified with respect to the central waveforms in the Intact and F2020 samples to determine the effect of intersections on time delays. The change in the relative arrival time for the intact sample (Fig. 13b) occurs because of the difference in the length of the travel path between the source and receiver (Fig. 14a). The source was held at a fixed location and the travel path increased as the receiver was translated away from the source position. Figure 14b, c shows the relative time delays along a vertical line through the center of the wave front and through a vertical fracture that is 10 mm from the wave front center, respectively. The relative time delays in Fig. 14b, c were corrected for the geometric delay by subtracting the relative delay measured on the intact sample from the values for the fractured sample. In Fig. 14b, the relative time delay is zero for positions from −8 mm to +8 mm because the waves recorded between these positions only traveled in the intact portion of sample F2020. When a wave propagated across a fracture (positions −10 mm and +10 mm), the signal was delayed. The delay decreases for signals recorded below −10 mm and above 10 mm because the time delay decreases as the angle of incidence on the fracture increases (Pyrak-Nolte et al. 1990a). As the fractures closed under stress, the time delay across the fractures decreased.

A comparison of the group time delays for a single fracture, two fractures, and two fracture intersections is
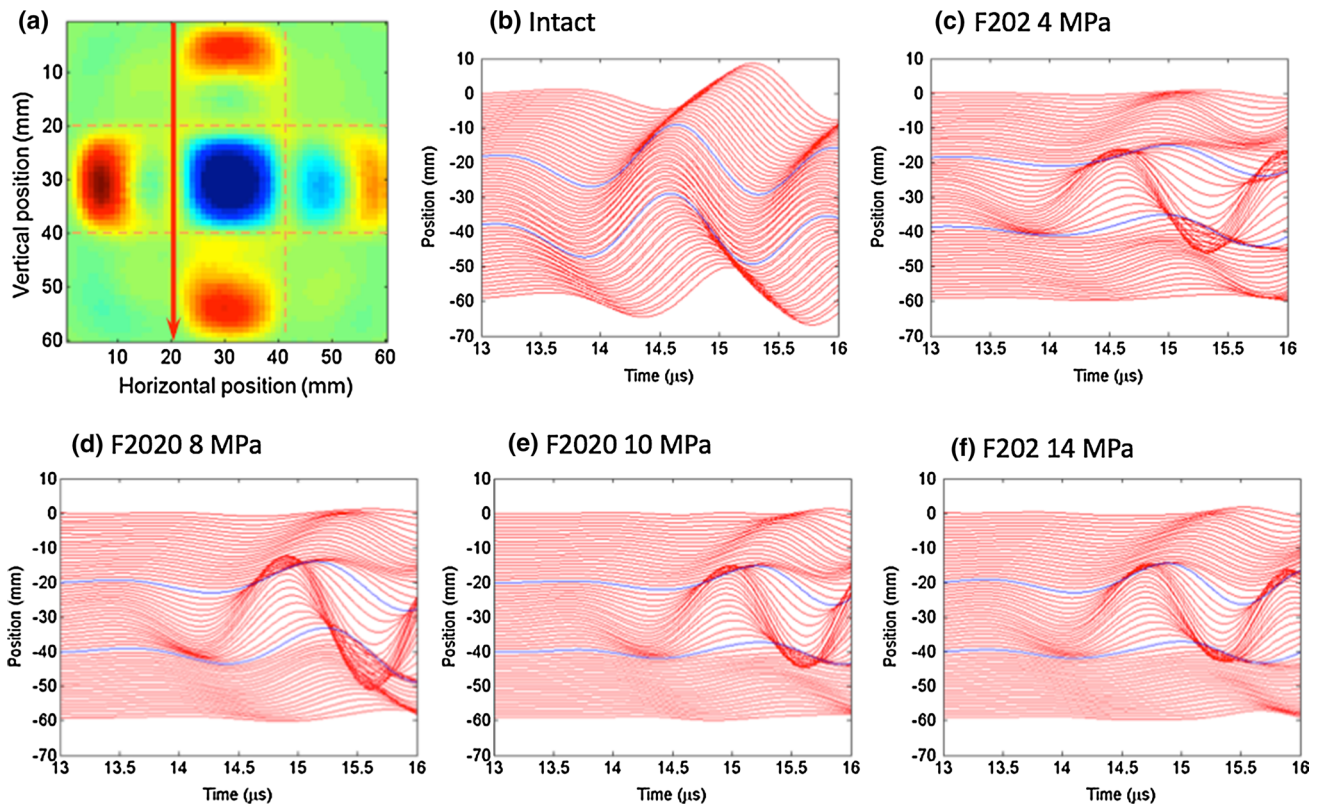
Fig. 13 Compressional wave signals from the recorded wave front taken at receiver positions along **a** a vertical line 10 mm from the center of the sample (indicated by the *red arrow*) from the **b** the intact sample, and **c–f** sample F2020 for bi-axial stresses that ranged form 4–14 MPa (color figure online)
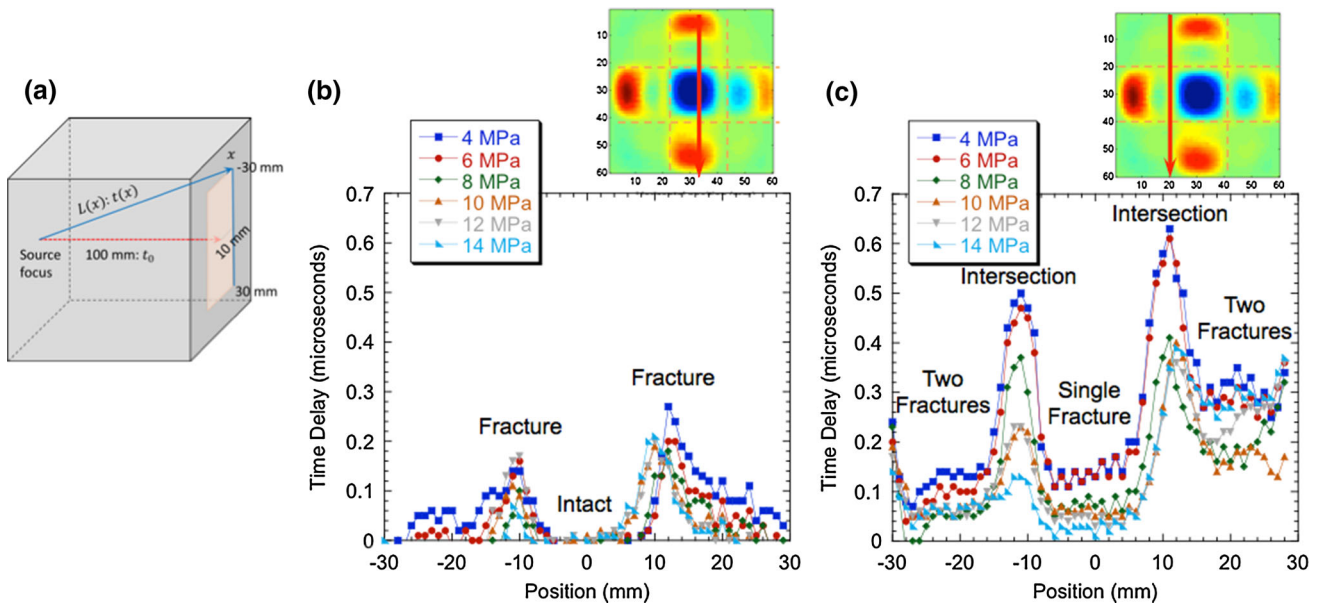
Fig. 14 a Geometry used to calculate relative time delay across, **b** single fractures, and **c** across a single fracture and fracture intersections. The *red arrow* indicates the direction of the position axis (color figure online)

given in Fig. 14c. The geometrically corrected relative time delays are shown for signals recorded along a vertical fracture that is 10 mm from the wave front center (see inset

in Fig. 14c). Signals for positions from −8 mm to +8 mm propagated across a single fracture, while signals from positions less than −14 mm and greater than +14 mm

propagated across two fractures (one horizontal and one vertical). As bi-axial stress was increased on the sample, the signal delay decreased across the fractures as fracture-specific stiffness increased. The specific stiffness of the fractures varied by a factor of 2.5 between the delays measured across the two fractures for positions less than −14 mm and for those greater than +14 mm. This difference in fracture-specific stiffness is consistent with the observation of larger amplitudes in the lower left corner of the snapshots of the wavefronts for sample F2020 in Fig. 4c, d compared to the upper left region of the snapshots.

At low stress, the time delays observed at the intersections (positions −11 mm and +11 mm) are greater than twice the delay caused by a single fracture or by two fractures. At 4 and 6 MPa, the time delay from a single fracture was 0.14 μs, and from two fractures the delays were 0.14 and 0.3 μs. The group time delays for the two intersections were 0.5 and 0.6 μs, respectively, at low stress. As stress increased on the sample, the time delays decreased but a significant difference in delay at the intersections was still observed. This observation provides additional evidence that wave propagation across an intersection is sensitive to coupling or "stiffness" of an intersection. The large time delay observed in the measured data for the intersection most likely arises from the energy partitioning into, and interference among, transmitted waves, guided waves, and other scattered modes (see Sect. 4.1).

5 Conclusions

Elastic waves propagated through a medium with orthogonal fracture sets have signals that are rich in information related to fracture spacing, fracture-specific stiffness, and mechanical coupling along fracture intersections. However, interpretation of these signals requires the identification of possible guided modes that propagate along fractures, between fractures and along fracture intersections, and also requires an understanding of the effect of fracture intersections on body or bulk waves. From the data presented in this paper, intersections between fractures were observed to cause additional time delays and attenuation of the wave front that were larger than would be expected simply from the superposition of effects from two fractures acting alone. New theories for wave propagation in rock with orthogonal fracture sets are needed that account for energy partitioning, by the fractures and fracture intersections, into transmitted/reflected waves, guided modes and other scattered waves to explain the wave interference that gives rise to the strong delays and attenuation observed in the experimental data.

In addition, though the experiments were carried out under uniform bi-axial loading conditions, fracture stiffnesses differed by ∼30–70 % among fractures within and between fracture sets. Future theoretical work needs to account for variation in fracture stiffness among fractures within a network given the stress gradients in the Earth and non-uniform stress conditions caused by anthropogenic activities such as subsurface excavation, and extraction/storage of fluids. Finally, orthogonal fracture sets formed rectangular wave-guides that confined energy and generated leaky guided modes. The amount of energy that "leaks" out of a wave-guide depends on the frequency of the signal and the stiffness of the fractures that define the boundaries of the wave-guide. The arrival time and amplitude of these guided modes were affected by the shape of the rectangular wave-guide that was defined by the fracture spacings of the vertical and horizontal fractures sets. Further development of theoretical and numerical tools is needed to account for the effect of fracture intersections and non-uniform fracture stiffness on propagating waves through fractured media. Ignoring the effect of intersections on a propagating wave can lead to misinterpretation of fracture orientations, fracture-specific stiffness, and effective moduli for a fractured medium. If the observed large time delays from fracture intersections were interpreted as simply arising from fractures, the interpreted orientation of the fractures would be off 45° and affect the estimation of elastic constants used in engineering design analysis.

References

Abell BC (2015) Elastic Waves along a Fracture Intersection, Ph.D. thesis, Purdue University, West Lafayette, p 295

Abell BC, Pyrak-Nolte LJ (2013) Coupled wedge waves. J Acoust Soc Am 134(5):3551

Abell BC, Shao S, Pyrak-Nolte LJ (2014) Measurements of elastic constants in anisotropic media. Geophysics 79(5):D349–D362

Amadei B (1996) Importance of anisotropy when estimating and measuring in situ stresses in rock. Inter J Rock Mech Min Sci Geomech Abstr 33(3):293–325

Amadei B, Goodman RE (1982) The influence of rock anisotropy on stress measurements by overcoring techniques. Rock Mech 15:167–180

Angel YC, Achenbach JD (1985) Reflection and transmission of elastic waves by a periodic array of cracks. J Appl Mech 52:33–41

Bai TX, Maerten L, Gross MR, Aydin A (2002) Orthogonal cross joints: do they imply a regional stress rotation? J Struct Geol 24(1):77–88

Bakulin A, Grechka V, Tsvankin I (2000) Estimation of fracture parameters from reflection seismic data—P II: fractured models with orthorhombic symmetry. Geophysic 65(6):1803–1817

Braun MG, Kelemen PB (2002) Dunite distribution in the Oman ophiolite: Implications for melt flux through porous dunite conduits. Geochem Geophys Geosyst 3:1–21

Carcione JM, Picotti S (2012) Reflection and transmission coefficients of a fracture in transversely isotropic media. Stud Geophys Geod 56:307–322

Choi M-K, Bobet A, Pyrak-Nolte LJ (2014) The effect of surface roughness and mixed-mode loading on the stiffness ratio, Kx/Kz for fractures. Geophysics 79(5):D319–D331

Cook NGW (1992) Natural joints in rock: mechanical, hydraulic, and seismic behavior and properties under normal stress. Int J Rock Mech Min Sci 29:198–223

De Basabe JD, Sen MK, Wheeler MF (2010) Seismic wave propagation in fractured media. SEG technical program expanded abstracts 2011, SEG san antonio 2011 meeting, pp 2920–2924

Far ME, de Figueiredo JJS, Stewart RR, Castagna JP, Han D-H, Dyaur N (2014) Measurements of seismic anisotropy and fracture compliances in synthetic fractured media. Geophys J Int 197:1845–1857

Fuck RF, Tsvankin I (2006) Seismic signatures of two orthogonal sets of vertical microcorrugated fractures. J Seism Explor 15:183–208

Goodman RE, Taylor RL, Brekke TL (1968) A model for the mechanics of jointed rock. J Soil Mech Found Div Am Soc Civ Eng 94(SM3):637–659

Grechka V, Kachanov M (2006) Effective elasticity of fractured rocks: a snapshot of the work in progress. Geophysics 71(6):W45–W58

Greenwood JA, Williamson JB (1966) Contact of nominally flat surfaces. In: Proceedings of the royal society of london series a—mathematical physical and engineering sciences, p 295

Gross MR (1993) The origin and spacing of cross joints—examples from the Monterey formation, Santa Barbara Coastline, California. J Struct Geol 15(6):737–751

Gu BL (1994) Interface waves on a fracture in rock, Ph.D. thesis, University of California, Berkeley, Berkeley

Gu BL, Suarez-Rivera R, Nihei KT, Myer LR (1996) Incidence of plane waves upon a fracture. J Geophys Res 101(B11):25337–25346

Hauser MR, Weaver RL, Wolfe JP (1995) Internal diffraction of ultrasound in crystals: phonon focusing at long wavelengths. Phys Rev Lett 68(17):2604–2607

Hobday C, Worthington MH (2012) Field measurements of normal and shear fracture compliance. Geophys Prospect 60(3):488–499

Hodgson RA (1961) Regional study of jointing in Comb Ridge-Navajo Mountain area, Arizona and Utah. AAPG Bull 45(1):1–37

Hood JA, Schoenberg M (1989) Estimation of vertical fracturing from measured elastic moduli. J Geophys Res 94:15,611–615,618

Hopkins DL (1990) The effect of surface roughness on joint stiffness, aperture and acoustic wave propagation, Ph.D. thesis, University of California, Berkeley, Berkeley

Hopkins DL, Cook NGW, Myer LR (1990) Normal joint stiffness as a function of spatial geometry and surface roughness. In: Paper presented at international symposium on rock joints, Loen, Norway

Kendall K, Tabor D (1971) An ultrasonic study of the area of contact between stationary and sliding surfaces. Proc R Soc Lond Ser A 323:321–340

Lubbe R, Worthington MH (2006) A field investigation of fracture compliance. Geophys Prospect 54(3):319–331

Lubbe R, Sothcott J, Worthington MH, McCann C (2008) Laboratory estimates of normal and shear fracture compliance. Geophys Prospect 56(2):239–247

Mandl G (2005) Rock joints: the mechanical genesis. Springer, Berlin

Murty GS, Kumar V (1991) Elastic wave propagation with kinematic discontinuity along anon-ideal interface between two isotropic elastic half-spaces. J Nondestr Eval 10(2):39–53

Myer LR (2000) Fractures as collections of cracks. Int J Rock Mech Min Sci 37:231–243

Nagy PB, Bonner BP, Adler L (1995) Slow wave imaging of permeable rock. Geophys Res Lett 22(9):1053–1056

Nakagawa S (1998) Acoustic resonance characteristics of rock and concrete containing fractures, Ph.D. thesis, University of California, Berkeley

Nakagawa S, Nihei KT, Myer LR (2000a) Shear-induced conversion of seismic waves across single fractures. Int J Rock Mech Min Sci 37(1–2):203–218

Nakagawa S, Nihei KT, Myer LR (2000b) Stop-pass behavior of acoustic waves in a 1D fractured system. J Acoust Soc Am 107(1):40–50

Nakagawa S, Nihei KT, Myer LR (2002) Elastic wave propagation along a set of parallel fractures. Geophys Res Lett 29(16):31.1–31.4

Nihei KT, Myer LR, Cook NGW, Yi WD (1994) Effects of nonwelded interfaces on guided SH-waves. Geophys Res Lett 21(9):745–748

Nihei KT, Yi WD, Myer LR, Cook NGW, Schoenberg M (1999) Fracture channel waves. J Geophys Res Solid Earth 104(B3):4769–4781

Nolte DD, Pyrak-Nolte LJ, Beachy J, Ziegler C (2000) Transition from the displacement discontinuity limit to the resonant scattering regime for fracture interface waves. Int J Rock Mech Min Sci 37(1–2):219–230

Oliger A, Nolte DD, Pyrak-Nolte LJ (2003) Seismic focusing by a single planar fracture. Geophys Res Lett 30(5):1203

Petrovitch CL (2013) Universal scaling of the flow-stiffness relationship in weakly correlated single fractures. Ph.D. Purdue University, West Lafayette, IN

Petrovitch CL, Nolte DD, Pyrak-Nolte LJ (2013) Scaling of fluid flow versus fracture stiffness. Geophys Res Lett 40:2076–2080

Petrovitch CL, Pyrak-Nolte LJ, Nolte DD (2014) Combined scaling of fluid flow and seismic stiffness in single fractures. Rock Mech Rock Eng 47:1613. doi:10.1007/s00603-014-0591-z

Pyrak-Nolte LJ (1996) The seismic response of fractures and the interrelations among fracture properties. Int J Rock Mech Min Sci 33(8):787

Pyrak-Nolte LJ, Cook NGW (1987) Elastic interface waves along a fracture. Geophys Res Lett 14(11):1107–1110

Pyrak-Nolte LJ, Nolte DD (2016) Approaching a universal scaling relationship between fracture stiffness and fluid flow. Nat Commun 7:10663. doi:10.1038/ncomms10663

Pyrak-Nolte LJ, Myer LR, Cook NGW, Witherspoon PA (1987) Hydraulic and mechanical properties of natural fractures in low permeability rock. In: Paper presented at sixth international congress on rock mechanics, A. A. Balkema, Montreal, Canada

Pyrak-Nolte LJ, Myer LR, Cook NGW (1990a) Anisotropy in seismic velocities and amplitudes from multiple parallel fractures. J Geophys Res Solid Earth Planets 95(B7):11345–11358

Pyrak-Nolte LJ, Myer LR, Cook NGW (1990b) Transmission of seismic-waves across single natural fractures. J Geophys Res Solid Earth Planets 95(B6):8617–8638

Pyrak-Nolte LJ, Xu JP, Haley GM (1992) Elastic interface waves propagating in a fracture. Phys Rev Lett 68(24):3650–3653

Pyrak-Nolte LJ, Roy S, Mullenbach BL (1996) Interface waves propagated along a fracture. J Appl Geophys 35(2–3):79–87

Schoenberg M (1980) Elastic wave behavior across linear slip interfaces. J Acoust Soc Am 5(68):1516–1521

Schoenberg M, Douma J (1988) Elastic wave propagation in media with parallel fractures and aligned cracks. J Geophys Prospect 36:571–590

Schoenberg M, Helbig K (1997) Orthorhombic media: modeling elastic wave behavior in a vertically fractured earth. Geophysics 62:1954–1974

Shao S (2015) Fractures in anisotropic media, Ph.D. thesis, Purdue University, West Lafayette, p 228

Shao S, Pyrak-Nolte LJ (2013) Interface waves along fractures in anisotropic media. Geophysics 78(4):T99–T112

Shao S, Petrovitch CL, Pyrak-Nolte LJ (2015) Wave guiding in fractured layered media. In: Agar SM, Geiger S (eds) SP406 fundamental controls on fluid flow in carbonates: current workflows to emerging technologies, Geological Society of London, SP406 (in press)

Stearns DW (1972) Reservoirs in fractured rock. AAPG Spec Vol A010:82–106

Xian CJ, Nolte DD, Pyrak-Nolte LJ (2001) Compressional waves guided between parallel fractures. Int J Rock Mech Min Sci 38(6):765–776